

Efficient Energy Transfer in Light-Harvesting Systems: Quantum-Classical Comparison, Flux Network, and Robustness Analysis

Jianlan Wu,^{1,2} Fan Liu,² Jian Ma,¹ Robert J. Silbey*,² and Jianshu Cao^{†2}

¹Physics Department, Zhejiang University,

38 ZheDa Road, Hangzhou, Zhejiang, 310027, China

²Department of Chemistry, MIT, 77 Massachusetts Ave, Cambridge, MA, 02139, USA

(Dated: July 30, 2018)

arXiv:1109.5769v2 [physics.chem-ph] 5 Sep 2012

* dedicated to the memory of Prof. Robert J. Silbey

† E-mail: jianshu@mit.edu.

Abstract

Following the calculation of optimal energy transfer in thermal environment in our first paper (Wu *et al.*, *New J. Phys.*, 2010, **12**, 105012), full quantum dynamics and leading-order ‘classical’ hopping kinetics are compared in the seven-site Fenna-Matthews-Olson (FMO) protein complex. The difference between these two dynamic descriptions is due to higher-order quantum corrections. Two thermal bath models, classical white noise (the Haken-Strobl-Reineker model) and quantum Debye model, are considered. In the seven-site FMO model, we observe that higher-order corrections lead to negligible changes in the trapping time or in energy transfer efficiency around the optimal and physiological conditions (2% in the HSR model and 0.1% in the quantum Debye model for the initial site at BChl 1). However, using the concept of integrated flux, we can identify significant differences in branching probabilities of the energy transfer network between hopping kinetics and quantum dynamics (26% in the HSR model and 32% in the quantum Debye model for the initial site at BChl 1). This observation indicates that the quantum coherence can significantly change the distribution of energy transfer pathways in the flux network with the efficiency nearly the same. The quantum-classical comparison of the average trapping time with the removal of the bottleneck site, BChl 4, demonstrates the robustness of the efficient energy transfer by the mechanism of multi-site quantum coherence. To reconcile with the latest eight-site FMO model, the quantum-classical comparison with the flux network analysis is summarized in the appendix. The eight-site FMO model yields similar trapping time and network structure as the seven-site FMO model but leads to a more disperse distribution of energy transfer pathways.

I. INTRODUCTION

Natural photosynthesis is of particular interest due to its essential role as the energy source for life on earth. In the process of biological evolution over billions of years, photosynthetic systems have developed optimal and robust strategies of converting solar energy to chemical energy. In the early stage of photosynthesis, solar energy is collected by pigments and transferred through light-harvesting protein complexes to the reaction center for the subsequent charge-separation. The energy conversion from photons to electrons is fast, robust, and nearly perfect in efficiency, although the overall efficiency of photosynthesis is low. Understanding the mechanism of efficient energy transfer in natural light-harvesting systems can help developing low-cost and highly-efficient man-made solar energy apparatus, including photovoltaic devices and artificial photosynthesis [1].

For a long time, energy transfer was considered as an incoherent process described by hopping kinetics with Forster rate constants. The Forster rate theory has been a prevailing theoretical technique. In spite of the widespread success of the Forster rate approach, recent experimental advance has shown evidence of long-lived quantum coherence in several natural light-harvesting systems, e.g., Fenna-Matthews-Olson (FMO) [2, 3] and phycocyanin 645 (PC645) [4]. A full quantum dynamic framework becomes necessary for studying coherent energy transfer. Many theoretical techniques have been developed to serve this purpose [5–30]. With temporal-spatial correlation for the protein environment, the generalized Bloch-Redfield (GBR) equation [5–9], the hierarchy equation [10–14], and other methods [16] have successfully predicted the long-lived quantum coherent phenomenon. Alternatively, the Haken-Strobl-Reineker (HSR) model and its generalization [17–19] have attracted much attention due to its simplicity, although the bath noise is classical [6, 20, 21, 23–26]. Recently, quantum-classical mixed methods have been also applied to the dynamics of energy transfer [28–30]. Different theoretical methods have been tested in the simple two-site system [11] and other complex systems [27], mainly focusing on the reliability of theoretical predictions.

However, a systematic and comprehensive investigation is still needed to distinguish hopping kinetics and full quantum dynamics, with the goal of quantifying nontrivial quantum effects, e.g., long-range quantum coherence, in a complex energy transfer network. Throughout this paper, the long-range quantum coherence is defined in the local site basis and excludes the contribution from the two-state quantum dynamics. Here we will propose a

quantum-classical comparison strategy, and apply it to the seven-site FMO system with two different descriptions of baths: the classical white noise (the HSR model) and the quantum Debye noise. In spite of their simplicity, quantum dynamics under these two bath models can be computed exactly and thus can be used for a meaningful quantum-classical comparison. Although the additional eighth site in the new eight-site FMO model can modify quantum dynamics, the seven-site model is a good example to explore interesting and relevant quantum phenomena, and it is also consistent with our previous paper [6]. In Appendix C, we will present a short summary on the eight-site FMO model. Here we will use the leading-order kinetics: a hopping network with Fermi’s golden rule rate, which is the leading-order expansion to quantum dynamics. With a dipole-dipole interaction between two chromophores, Fermi’s golden rule rate becomes Forster rate of energy transfer. In the standard fashion, such hopping kinetics is considered as a ‘classical’ description of energy transfer. In this paper, we will explore energy transfer in FMO using exact quantum dynamic equations and using Fermi’s golden rule rate (i.e., Forster rate) to quantify the difference between full quantum dynamics and ‘classical’ hopping kinetics. This difference includes nontrivial quantum effects, e.g., multiple-site coherence. A systematic kinetic mapping of quantum dynamics including high-order corrections was described in a review paper for the classical noise [20] and will be described for the quantum noise in a forthcoming publication [31].

In the first paper of this series [6], we applied the HSR model and the GBR equation approach to optimize energy transfer with intermediate values for various bath parameters, such as reorganization energy, bath relaxation rate, temperature, and spatial correlation. In particular, we found an optimal temperature for efficient energy transfer in the seven-site FMO model. Our results have been verified by the hierarchic equation [32]. The optimization behavior has been found in other conditions such as the spatial arrangement [8]. The site energy optimization for the new eight-site FMO model is shown in the third paper of this series [9]. To interpret the optimization behavior, we have proposed the concept of trapping-free subspace, and determined the asymptotic scalings in the weak and strong dissipation limits [33]. Since two-site quantum coherence is included in Fermi’s golden rule rate, ‘classical’ hopping kinetics can predict the optimization behavior in many light-harvesting systems, as we will show in this paper. Therefore, the quantum-classical comparison reported in this paper is essential for identifying the contribution of nontrivial quantum effects to optimal energy transfer. Specifically, we will investigate two quantities: the trapping time and the

branching probability. The former is directly related to the energy transfer efficiency as shown in our first paper [6], whereas the latter is a new concept constructed by directional population flux for each two-site pair in the energy transfer network [34–36]. A key advantage of natural photosynthesis compared to its artificial counterpart is the robustness against environmental variation and self-protection against damages. Here the quantum-classical comparison is combined with the stability analysis of energy transfer to quantify the robustness in FMO. Our study thus provides a new approach to understand the biological role of nontrivial quantum effects excluding the two-site coherence, different from other theoretical papers on time-dependent behaviors of quantum coherence and entanglement [37].

The paper is organized as follows: In Sec. II, we review the quantum dynamic framework for light-harvesting energy transfer. In Sec. III, we use the leading order of kinetic mapping to define ‘classical’ hopping kinetics, and introduce the concept of the integrated population flux and the branching probability. In Secs. IV-V, we apply the HSR model and compare the trapping times and the branching probability in the flux networks of FMO calculated from the classical hopping kinetics and full quantum dynamics. The sensitivity of parametric dependence for the trapping time is evaluated using classical hopping kinetics. The robustness of energy transfer is explored by removing one donor site of FMO together with a quantum-classical comparison. In Sec. VI, we apply the Debye spectral density for the protein environment. The trapping time and the flux network are computed quantum mechanically using the hierarchy equation and classically using Fermi’s golden rule rate. In Sec. VII, we conclude and discuss our results of quantum-classical comparison and robustness analysis. The necessary mathematical formulation is provided in Appendices A and B. A short summary of the eight-site FMO model is given in Appendix C with emphasis on the quantum-classical comparison and the flux network analysis.

II. LIOUVILLE DYNAMICS AND TRANSFER EFFICIENCY

In this section, we review the theoretical framework of exciton dynamics, following the same notation as introduced in a previous review article [20] and the first paper of this three-part series [6].

For each local chromophore (site) of the exciton system, a two-level truncation is reliable

for the lowest electronic excitation. In consistence with low light absorption in natural light-harvesting systems, we consider the situation of single excitation, and then energy transfer dynamics can be studied in the subspace of single-excitation quantum states. Thus, we introduce a tight-binding Hamiltonian in the site ($\{|n\rangle\}$) representation [38],

$$H = \sum_n \varepsilon_n |n\rangle\langle n| + \sum_{m \neq n} J_{mn} |m\rangle\langle n|, \quad (1)$$

where ε_m is the excitation energy at chromophore site m and J_{mn} is the electronic coupling strength between the m -th and n -th sites. The system investigated in this paper is the Fenna-Matthews-Olson (FMO) protein complex with seven bacteriochlorophyll (BChl) sites [2, 3, 39–44]. To be consistent, we use the particular Hamiltonian model in our first paper [6]. The possibility of the eighth site in FMO has been addressed recently [45], and the optimization of energy transfer regarding the new FMO model is studied in the third paper of this series [9].

For an exciton system, the time evolution of the reduced density matrix $\rho(t)$ is governed by the Liouville equation [20, 38, 46, 47],

$$\dot{\rho}(t) = -[\mathcal{L}_{\text{sys}} + \mathcal{L}_{\text{trap}} + \mathcal{L}_{\text{decay}} + \mathcal{L}_{\text{dissp}}] \rho(t). \quad (2)$$

The four Liouville superoperators \mathcal{L} on the right-hand side of the above equation correspond to four distinct dynamic processes, which are discussed as follows. For an isolated system, the system Liouville superoperator \mathcal{L}_{sys} is given by the commutator of the system Hamiltonian, $\mathcal{L}_{\text{sys}}\rho = i[H, \rho]$, and its explicit form in the Liouville space is

$$[\mathcal{L}_{\text{sys}}]_{mn,kl} = i(H_{mk}\delta_{n,l} - H_{ln}\delta_{m,k}). \quad (3)$$

For conciseness, we neglect the reduced Planck constant \hbar throughout this paper.

The irreversible population depletion of the exciton system originates from exciton decay by the electron-hole recombination and energy trapping at the reaction center [6, 20]. The Liouville superoperators of these two processes are diagonal: $[\mathcal{L}_{\text{decay}}]_{mn} = k_{d,mn} = (k_{d,m} + k_{d,n})/2$, and $[\mathcal{L}_{\text{trap}}]_{mn} = k_{t,mn} = (k_{t,m} + k_{t,n})/2$, where $k_{d,n}$ and $k_{t,n}$ are phenomenological decay and trapping rate constants at site n , respectively. Here $[\mathcal{L}]_{mn} = [\mathcal{L}]_{mn,mn}$ represents the diagonal element. In practice, we often assume a homogeneous decay process with $k_{d,n} = k_d$. In the FMO system, BChl 3 is the trap site connecting to the reaction center, $k_{t;n} = k_t\delta_{n,3}$, and the trapping rate is set to be $k_t = 1 \text{ ps}^{-1}$.

In addition to the above three dynamic processes, the excitation energy transfer is modulated by fluctuations due to the interaction between the exciton system and the protein environment. On the microscopic level, $\mathcal{L}_{\text{dissp}}$ is evaluated using the explicit system-bath Hamiltonian. Within this description, the linearly-coupled harmonic bath, $H_{SB} = \sum_n |n\rangle\langle n|B_n$, is widely applied, with B_n the linear quantum operator of bath [38, 46, 47]. The dissipative dynamics of system is then fully determined by the bath spectral density $J(\omega)$. For simplicity, we ignore the spatial correlation of bath in this paper and discuss its effect in the future. Next we can apply quantum dynamic methods, e.g., the Redfield equation, the generalized Bloch-Redfield equation [5–9], and the Forster equation, under various approximations. For a Gaussian bath whose time correlation function can be represented as a linear combination of exponentially decaying functions, the hierarchy equation approach can provide a reliable prediction of quantum dynamics [10–12].

Alternatively, we can view the system-bath interaction as a time-dependent fluctuation on the system Hamiltonian [10, 17–19, 48], i.e., $H(t) = H + \delta H(t)$, with $\langle \delta H(t) \rangle = 0$. The dissipative dynamics can be fully determined if all the time-averaged moments of $\delta H(t)$ are resolved, which is usually an unfeasible task. In the extremely high temperature limit, $\delta H(t)$ behaves classically and the relevant second-order moment becomes real. One example of this approximation is the HSR model where a classical white noise, $\langle \delta \varepsilon_m(t) \delta \varepsilon_n(0) \rangle = \Gamma^* \delta_{m,n} \delta(t)$, is assumed on site energies [17, 18]. The dissipation Liouville superoperator becomes diagonal in the site representation, $[\mathcal{L}_{\text{dissp}}]_{mn} = (1 - \delta_{m,n})\Gamma^*$, where Γ^* is the pure dephasing rate. Since the HSR model can be rigorously solved, it serves as the simplest model to examine our kinetic mapping of quantum dynamics.

A key quantity of excitation energy transfer is the energy transfer efficiency q , which is the ratio of energy trapping at the reaction center. The mathematical definition of q is given by

$$q = \int_0^\infty dt \text{Tr} \{ \mathcal{L}_{\text{trap}} \rho(t) \} = \sum_n k_{t;n} \tau_n, \quad (4)$$

where τ_n is the mean residence time at site n , $\tau_n = \int_0^\infty dt \rho_n(t)$. For an arbitrary vector X in Liouville space (e.g., the density matrix ρ), its trace is defined as $\text{Tr}\{X\} = \sum_n X_{nn}$. In nature, spontaneous energy decay occurs on the time scale of nanosecond, much slower than the picosecond energy transfer process. The condition of $k_d \approx 1 \text{ ns}^{-1} \ll k_t$ allows us

to simplify the transfer efficiency to [6, 20],

$$q \approx \frac{1}{1 + k_d \langle t \rangle}, \quad (5)$$

where $\langle t \rangle = \sum_n \tau_n(k_d = 0)$ is the mean first passage time to the trap state in the absence of decay (i.e., the average trapping time). The comparison of transfer efficiencies calculated from Eqs. (4) and (5) has been examined in our first paper [6], and their excellent agreement over a broad range of Γ^* proves the reliability of Eq. (5). In this paper, we will ignore the energy decay process and focus on the average trapping time $\langle t \rangle$. Following the formal solution of Eq. (2), the average trapping time,

$$\langle t \rangle = \text{Tr} \{ \mathcal{L}^{-1} \rho(0) \}_{k_d=0}, \quad (6)$$

is determined by the Liouville superoperator $\mathcal{L} = \mathcal{L}_{\text{sys}} + \mathcal{L}_{\text{trap}} + \mathcal{L}_{\text{dissp}}$ and the initial condition $\rho(0) = \rho(t = 0)$. For the FMO system, BChl 1 and BChl 6 connected to the baseplate are considered as two initial sites for energy transfer [12]. In our calculation, we consider two initial conditions at either BChl 1 ($\rho_1(0) = 1$, initial condition I) or BChl 6 ($\rho_6(0) = 1$, initial condition II).

III. KINETIC MAPPING, FLUX NETWORK, AND BRANCHING PROBABILITY

A. Kinetic Mapping

In our first paper, we have demonstrated the generality of optimal energy transfer by the competition of quantum coherence and bath-induced relaxation [6]. A remaining question is to identify contributions of nontrivial quantum effects. To do this, we systematically map the energy transfer process to a kinetic process. With the Markovian approximation, the quantum kinetic equation reads [20]

$$\dot{P}_m = - \sum_{n \neq m} (k_{mn}^Q P_m - k_{nm}^Q P_n) - k_{t,m} P_m, \quad (7)$$

where $P_m = \rho_{mm}$ is the population at site m . The effective quantum kinetic rate k_{mn}^Q can be formally derived following the Laplace transformation, as shown in Appendix A. In the HSR model, the kinetic mapping is solved in a recent feature article [20], following an

alternative stationary approximation for quantum coherence $\rho_{mn}(t)$. In a general quantum network, the kinetic mapping in a rigorous non-Markovian form will be left in a forthcoming paper [31]. The formal derivation in Appendices A and B is sufficient for understanding quantum-classical comparison in this paper. Equation (7) can be organized into a matrix form as $\dot{P} = -(K^Q + K_t)P$, where $[P]_m = P_m$ is the population vector. The two rate matrices, K^Q and K_t , are defined as $[K^Q]_{m,n(\neq m)} = -k_{m,n}^Q$, $[K^Q]_{n,n} = \sum_{m(\neq n)} k_{m,n}^Q$, and $[K_t]_{m,n} = \delta_{m,n}k_{t;n}$. The average trapping time can be alternatively defined as

$$\langle t \rangle = \sum_n \tau_n = \sum_n [(K^Q + K_t)^{-1}P(0)]_n. \quad (8)$$

which is exactly the same as that in Eq. (6).

In this kinetic mapping, the leading order term represents the ‘classical’ hopping behavior in the site basis, and higher-order corrections represent nontrivial quantum coherent effects. In practice, the full quantum kinetic rates K^Q are difficult to evaluate exactly whereas the leading-order hopping rates K^C can be calculated using Fermi’s golden rule expression [31]. For the ‘classical’ hopping kinetics, the rate equation in Eq. (7) and the trapping time in Eq. (8) remain the same after the replacement of the classical rate matrix K^C . To distinguish quantities calculated by full quantum dynamics and by classical hopping kinetics, we denote the quantum results by $\{\tau_n^Q, \langle t \rangle_Q\}$ and the classical results by $\{\tau_n^C, \langle t \rangle_C\}$. The difference between the two trapping times is attributed to higher-order quantum corrections, e.g., multi-site quantum coherence.

B. Integrated Population Flux

To further reveal the difference between quantum and classical energy transfer, we construct the flux network defined by directional population flows [34–36]. For a classical kinetic network, the integrated population flux F_{mn}^C is defined by the net population flow from site n to site m ,

$$F_{mn}^C = k_{mn}^C \tau_n^C - k_{nm}^C \tau_m^C = \int_0^\infty k_{mn}^C P_n^C(t) - k_{nm}^C P_m^C(t) dt. \quad (9)$$

The quantum population flux F_{mn}^Q can be similarly defined by replacing the classical residence time τ_n^C and the hopping rate k^C with the quantum residence time τ^Q and the effective quantum rate k^Q from the kinetic mapping. Alternatively, we will rewrite F_{mn}^Q in terms of

the coherence decay time, $\tau_{mn}^Q = \int_0^\infty dt \rho_{mn}(t)$. As derived in detail in Appendix B, the quantum integrated population flux is given by

$$F_{mn}^Q = k_{mn}^Q \tau_n^Q - k_{nm}^Q \tau_m^Q = 2 \operatorname{Im} [J_{mn} \tau_{nm}^Q]. \quad (10)$$

Equations (9) and (10) will be used in this paper to calculate the population fluxes in the leading-order hopping kinetics and in full quantum dynamics, respectively, and their difference will reveal nontrivial quantum effects that cannot be revealed by the average trapping time $\langle t \rangle$ or efficiency.

C. Basic Properties of Flux Network

The concept of the integrated population flux is important in understanding network structure and dynamics. The classical flux was introduced in the study of enzymatic networks. Its quantum mechanical counterpart share many of the basic properties:

- Integrated flux accounts for the net population transfer in energy transfer processes. It vanishes for an equilibrium system because of the detailed balance condition and is an intrinsic property of non-equilibrium steady state (NESS) systems. Light-harvesting energy transfer is an irreversible NESS process driven by absorbed photons to the reaction center and is therefore characterized by the integrated flux.
- The flux is a conserved quantity which is normalized to unity for every absorbed photon. For a one-dimensional chain system, the flux is unit for every link, both in classical kinetics and in quantum dynamics. As a result, the integrated flux is a unique quantity to characterize the topology of an energy transfer network and to compare the quantum and classical flows in the network.
- The conservation of the integrated flux applies both globally and locally. For any state on the network, the sum of fluxes is zero, $\sum_m F_{mn} = 0$, so that the sum of fluxes into the state is identical to the sum of fluxes out of the state. As a result, we can define the branching probability,

$$q_{mn} = \frac{F_{mn}}{\sum_{m', F_{m'n} > 0} F_{m'n}}, \quad (11)$$

to describe the normalized probability of $n \rightarrow m$ from the starting point n . The complete set of q_{mn} then characterizes the flow pattern on the network. In the rest of this paper, the integrated population flux F_{mn} will be used interchangeably with the branching probability q_{mn} .

- In a kinetic network, the integrated population flux F_{mn} and the residence time τ_n can be simultaneously solved by imposing the flux conservation relationship (i.e., the flux balance approach) [34, 35]. This flux method can significantly reduce the computational cost for a large-scale network. As shown in the study of FMO in this paper, we will use the sign and magnitude of F_{mn} to quantify the reaction pathways in an irreversible network.

IV. QUANTUM-CLASSICAL COMPARISON IN THE HAKEN-STROBL-REINEKER MODEL

A. Trapping Time

For the HSR model, the quantum dynamics of the seven-site FMO system has been solved in our first paper [6]. Following the kinetic mapping, the 'classical' hopping rate between sites m and n is given by [20, 49]

$$k_{mn}^C = k_{nm}^C = \frac{2\Gamma_{mn}}{\Gamma_{mn}^2 + \Delta_{mn}^2} |J_{mn}|^2, \quad (12)$$

where the site energy difference is $\Delta_{mn} = \varepsilon_m - \varepsilon_n$ and the overall dephasing rate is $\Gamma_{mn} = \Gamma_{mn}^* + k_{t;mn}$. In Appendix A, we further prove that Eq. (12) can be recovered from Fermi's golden rule rate under a classical white noise. Next we calculate the trapping time in both full quantum dynamics and classical hopping kinetics. In Ref. [20], we have proven that $\langle t \rangle_Q$ and $\langle t \rangle_C$ are the same for the two-site system in the HSR model. Thus, the difference between these two trapping times arises from multi-site quantum coherence.

In Fig. 1, we plot the average quantum trapping time $\langle t \rangle_Q$ and the classical counterpart $\langle t \rangle_C$ as functions of the pure dephasing rate Γ^* with the two initial conditions for the seven-site FMO system. We observe that the values of $\langle t \rangle$ computed from the two different methods are close. For example, the relative difference between $\langle t \rangle_Q$ and $\langle t \rangle_C$ is 2% under the optimal condition of $\Gamma_{\text{opt}}^* = 175 \text{ cm}^{-1}$ for the initial population at BChl 1, while the

difference becomes less than 1% under $\Gamma_{\text{opt}}^* = 195 \text{ cm}^{-1}$ for the initial population at BChl 6. Overall, the relative trapping time difference is always less than 10% for $\Gamma^* \gtrsim 30 \text{ cm}^{-1}$.

Our result shows that full quantum dynamics and hopping kinetics lead to similar behaviors in the trapping time and energy transfer efficiency around the optimal condition. In the HSR model, energy transfer in the seven-site FMO is controlled by the downhill pathway from BChl 6 to BChl 3, which does not need long-range exchange assisted by multi-site quantum coherence [43]. More importantly, the trapping time is the sum of residence time at all the sites so that the cancelation from different sites can reduce the quantum effect. Unlike the classical white noise, a quantum colored noise at a finite temperature complicates the quantum-classical comparison, which will be discussed in Sec. VI.

B. Flux Network

In this subsection, we present the quantum-classical comparison of the population flux for the seven-site FMO system in the HSR model. For the two-site system in the HSR model, we can prove that Eqs. (9) and (10) lead to the same result, consistent with the result of the trapping time. In the over-damped limit, i.e., $\Gamma^* \gg |J|$, quantum dynamics reduces to classical hopping kinetics, and the two definitions become identical for multi-site networks. Apart from this limit, we compare the results obtained with Eqs. (9) and (10), and use their difference to define the higher-order contribution, e.g., multi-site quantum coherence in the HSR model.

Figure 2 presents relevant population fluxes (> 0.05) calculated by full quantum dynamics (F_{mn}^Q) and hopping kinetics (F_{mn}^C), with two initial conditions in FMO. For each initial condition, its respective optimal pure dephasing rate Γ_{opt}^* is used. Both quantum and classical flux networks show two identical dominating pathways: $1 \rightarrow 2 \rightarrow 3$ (path A) and $6 \rightarrow (5, 7) \rightarrow 4 \rightarrow 3$ (path B). This result is consistent with 2D electronic spectroscopy [43]. With initial condition II, path A is nearly negligible whereas with initial condition I, path B contributes significantly with $F_{34}^Q = 0.40$ ($F_{34}^C = 0.56$). As shown in the next section, the two-pathway structure in FMO helps maintain its high efficiency even if one donor is removed.

Compared to results of the average trapping time, the quantum-classical difference of fluxes is much larger. For the branching probability from BChl 1 to BChl 3, the weak

electronic coupling J_{13} leads to a small value of $F_{31}^C = 0.053$ in the hopping picture with initial condition I. On the other hand, multi-site quantum coherence allows the long-range population transfer through interconversion between various off-diagonal elements of the density matrix [31, 47]. This quantum tunneling effect enhances the quantum branching probability more than twice, $F_{31}^Q = 0.123$. For the entire network, we introduce the weighted relative difference between classical and quantum branching probabilities as

$$\chi_F = \frac{2 \sum_{m \neq n} |F_{mn}^Q - F_{mn}^C|}{\sum_{m \neq n} |F_{mn}^Q + F_{mn}^C|}. \quad (13)$$

The result is $\chi_F = 26\%$ for initial condition I and $\chi_F = 7\%$ for initial condition II. Both values are significantly larger than those for the trapping time ($\leq 2\%$). The comparison of population fluxes quantifies the contribution of multi-site quantum coherence in the HSR model.

The quantum-classical comparison of branching probabilities clarifies the structure of various energy transfer pathways. For the first path of $1 \rightarrow 2 \rightarrow 3$, our Hamiltonian shows that BChl 2 is the energy barrier along the transfer pathway. As we discussed, the quantum tunneling effect is relevant, assisting energy transfer. For the second pathway of $6 \rightarrow (5, 7) \rightarrow 4 \rightarrow 3$, the energy downhill structure allows quick energy transfer even in the classical hopping picture, and quantum effect is less relevant. The weighted relative flux difference χ_F is much larger in initial condition I than that in initial condition II, consistent with energy structures of these pathways.

V. ROBUSTNESS OF ENERGY TRANSFER IN THE HAKEN-STROBL-REINEKER MODEL

A. Stability Against the Variation of System/Bath Parameters

The leading-order kinetic network provides a simple estimate of the parametric dependence of the average trapping time and can explain the robustness of energy transfer via the insensitivity to changes in dephasing rate, trapping rate, and system Hamiltonian. Within the kinetic network, estimation based on the magnitudes of the hopping rate and trapping rate yields the average trapping time on the order of picosecond time scale, $\langle t \rangle \sim 10$ ps. In comparison with the average decay rate on the nanosecond time scale, $k_d = 1 \text{ ns}^{-1}$, the

| Site Removed | 1 | 2 | 4 | 5 | 6 | 7 | complete FMO |
|---|------|-------|-------|------|-------|------|--------------|
| $\langle t \rangle_C$ (initial condition I) (ps) | | 10.57 | 15.32 | 9.60 | 10.61 | 9.38 | 10.30 |
| $\langle t \rangle_Q$ (initial condition I) (ps) | | 10.32 | 12.41 | 9.17 | 9.84 | 9.13 | 10.10 |
| $\langle t \rangle_C$ (initial condition II) (ps) | 7.47 | 7.61 | 16.12 | 7.98 | | 7.78 | 8.72 |
| $\langle t \rangle_Q$ (initial condition II) (ps) | 7.51 | 7.72 | 14.31 | 7.80 | | 7.63 | 8.66 |

TABLE I: The quantum ($\langle t \rangle_Q$) and classical ($\langle t \rangle_C$) trapping times of FMO with the removal of one non-trapping site under the respective optimal dephasing rate for two initial conditions in the HSR model. As a comparison, the results for the complete seven-site model are shown in the last column.

average trapping rate is much faster and therefore the efficiency is close to one, $q \sim 1$. The small ratio of the trapping time and decay time, $k_d \langle t \rangle \sim 0.01$, suggests that significant drop in energy transfer efficiency will result from a change of two-order's magnitude in the trapping time. According to Eq. (12), changes of two-order's magnitude in Γ^* and k_t or changes of one-order's magnitude in the J and Δ disorders are needed to produce this drop, based on simple estimation. Although the above simple estimation can deviate from the rigorous quantum dynamics, our method reveals that FMO can resist a large change in dephasing rate, trapping rate, and system Hamiltonian, mainly because of the time scale separation between the decay process ($\mathcal{L}_{\text{decay}}$) and the other three dynamic processes (\mathcal{L}_{sys} , $\mathcal{L}_{\text{dissp}}$, and $\mathcal{L}_{\text{trap}}$).

B. Robustness Against the Loss of a BChl Chromophore

Over the course of evolution, the FMO complex has achieved robustness such that the high energy transfer efficiency is retained even if one or two chromophores do not function properly [50]. We investigate this feature by taking out one non-trapping site off the seven-site FMO network and then calculating the average trapping time under the optimal condition. As shown in Table I, removal of BChl 4 causes a noticeable increase in the average trapping time while removal of any other site do not have major effects and some can even enhance the transfer efficiency. The flux distribution in Fig. 2 indicates that BChl 4 is the bottleneck of the dominant pathway $6 \rightarrow (5, 7) \rightarrow 4 \rightarrow 3$, where all fluxes in this pathway converge to site 4 before arriving at the trap site. However, even with BChl 4 removed, the

increase in the average trapping time (or equivalently the decrease in efficiency) is moderate. This phenomenon is due to the two major pathways in the energy transfer network of FMO. Without multiple pathways in energy transfer networks, a linear-chain system exhibits much stronger response since the single pathway would be blocked after the removal of a donor. In addition, the trapping time decreases 12-20% (see Table I) in full quantum dynamics than in classical hopping kinetics, which demonstrates that the quantum coherence can help the FMO system further resist the damage on BChl 4. Next we plot the relation of $\langle t \rangle - \Gamma^*$ in Fig. 1 using both quantum dynamics and hopping kinetics for the FMO system with BChl 4 removed. Our results show that the quantum trapping time is consistently smaller than the classical result when BChl 4 is removed, verifying the robustness of energy transfer due to multi-site quantum coherence.

VI. QUANTUM-CLASSICAL COMPARISON IN A QUANTUM NON-MARKOVIAN BATH

In a general quantum network, the leading-order hopping rate is the same as Fermi's golden rule rate, which becomes the Forster rate if the dipole-dipole interaction J_{mn} is applied. In detail, Fermi's golden rule rate is written as

$$k_{m \neq n}^C = 2|J_{mn}|^2 \text{Re} \int_0^\infty dt e^{i\Delta_{mn}t} e^{-[g_{mn}(t) + k_{t;mn}t]}, \quad (14)$$

and

$$g_{mn}(t) = 2(1 - c_{mn}) \int_0^\infty d\omega \frac{J(\omega)}{\omega^2} [\coth(\beta\omega/2)(1 - \cos \omega t) + i \sin \omega t], \quad (15)$$

where $\beta = 1/k_B T$, $J(\omega)$ is the bath spectral density, and c_{mn} is the bath spatial correlation between sites m and n . The negative correlation $c_{mn(\neq m)} = -1$ is used in the spin-boson model, and the zero spatial correlation $c_{mn} = \delta_{m,n}$ is considered in this paper. Consistent with our first paper [6], we use the Debye spectral density,

$$J(\omega) = \Theta(\omega) \frac{2\lambda}{\pi} \frac{\omega D}{\omega^2 + D^2}, \quad (16)$$

with $\Theta(\omega)$ the step function, λ the reorganization energy, and D the Debye frequency. The real bath spectral density of the protein environment in FMO is more complicated with high-frequency signature of local vibrational modes. The approximate Debye spectral density, however, can predict reasonably well for the light spectra of FMO. Besides, quantum

dynamics is extremely difficult to be calculated rigorously for a complex bath spectral density. Therefore, we will keep the simple Debye spectral density in this paper. Without trapping, the ratio of forward and backward hopping rate constants satisfies the detailed balance condition, $k_{mn}^C/k_{nm}^C = \exp[-\beta(\varepsilon_n - \varepsilon_m)]$. The hopping rates from Eq. (14) are then used to compute the trapping time and population fluxes in ‘classical’ kinetics.

Applying the Matsubara expansion [38], the bath time correlation function $C(t)$ of the Debye spectral density follows

$$C(t) = \sum_{j=0}^{\infty} (f_j^r + i f_j^i) e^{-\nu_j t}, \quad (17)$$

where the zeroth decay rate is $\nu_0 = D$ and all the other decay rates are the Matsubara frequencies $\nu_{j \geq 1} = 2\pi j/\beta$. The coefficients f_j^r and f_j^i can be determined accordingly [12]. For the exponentially decaying bath, quantum dynamics can be reliably solved by the hierarchy equation approach in principle [10–13]. Here we use the explicit form shown in Ref. [12], with the trapping Liouville superoperator $\mathcal{L}_{\text{trap}}$ included for both the reduced density matrix and auxiliary fields. To reduce the computation cost, the high-temperature approximation, $\coth(\beta\omega/2) \approx 2/\beta\omega$, is applied so that all the Matsubara frequencies $\nu_{j \geq 1}$ are ignored in Eq. (17). To be consistent, the same approximation is used in computing hopping rates. The high-temperature approximation will not cause a significant difference in our calculation at room temperature ($T = 300$ K). Our quantum computation is truncated upto the 10th hierarchic order. Due to instability of Liouville superoperators, τ^Q is evaluated by the time integral of $\rho(t)$ for $\lambda \geq 15$ cm⁻¹. The resulting trapping time and population fluxes correspond to full quantum dynamics.

A. Trapping Time

Here we study the quantum-classical comparison with the change of λ by fixing $T = 300$ K and $1/D = 50$ fs. The dependence on other parameters can be explored similarly. Figure 3 presents the results of the trapping time computed using both quantum dynamics ($\langle t \rangle_Q$) and hopping kinetics ($\langle t \rangle_C$) with two distinct initial conditions in the seven-site FMO model. We observe that $\langle t \rangle_Q$ and $\langle t \rangle_C$ are still close, 0.1% and 11% under the physiological reorganization energy $\lambda = 35$ cm⁻¹, for the initial conditions I and II, respectively. Full quantum dynamics does not necessarily lead to a faster energy transfer process. With initial

condition I, $\langle t \rangle_Q$ is smaller than $\langle t \rangle_C$ for $\lambda > 34 \text{ cm}^{-1}$; with initial condition II, $\langle t \rangle_Q$ is larger than $\langle t \rangle_C$ in the complete range of λ . The latter behavior is consistent with a recent calculation of energy transfer rate in the two-site system [11].

To understand our quantum-classical comparison, we need to clarify higher-order corrections to the leading-order hopping kinetics in a quantum network at finite temperatures. (1) As shown in the HSR model, the first effect arises from multi-site quantum coherence, which facilitates the barrier-crossing energy transfer. This effect is beyond the Fermi golden rule rate (or the second-order truncation in a general manner) and arises from direct inter-conversion of various off-diagonal elements of the reduced density matrix. The multi-site quantum coherence, including tunneling, interference, and delocalization, has been discussed before [6, 12, 20, 51] and is now identified in the quantum-classical comparison. In a sense, our systematic expansion and flux network analysis provides quantitative measures to describe these effects. To distinguish from the two-site quantum coherence inherent in the Fermi's golden rule rate, we will use the concept of the multi-site quantum coherence to define nontrivial quantum effects throughout this paper. (2) The second effect comes from the non-Markovian bath. Without instantaneous bath relaxation, the system is retained in its previous state, slowing down energy transfer. In the second-order truncation method, a non-Markovian memory kernel can be still extracted, but the underlying Born approximation cannot capture the full contribution of bath relaxation. Following the Laplace transformation, we can prove that the results of τ and $\langle t \rangle$ are the same, calculated by Fermi's golden rule rate or the second-order non-Markovian master equation in the local basis. Hence, our comparison distinguishes higher-order effects of bath relaxation excluding the Born approximation. A systematic approach of including bath relaxation in electron transfer has been shown in Ref. [52]. (3) Other than the above two effects, a more subtle quantum-classical difference results from the steady-state population distribution. Without trapping, hopping kinetics always imposes $P_n(t \rightarrow \infty) \propto \exp(-\beta\varepsilon_n)$. Instead, the quantum steady-state distribution is evaluated by $\rho(t \rightarrow \infty) \propto \text{Tr}_B\{\exp(-\beta H_{\text{tot}})\}$, which arises from the rigorous quantum Boltzmann distribution with the consideration of both system and bath [53]. The steady-state population of the lowest energy trap site can be decreased, implying a lower probability of energy being trapped (energy transfer efficiency). The interplay of these three effects suggests that quantum energy transfer can be much more complicated, compared to the leading-order hopping kinetics. The identification of various higher-order effects for the

trapping time and transfer efficiency will be studied in our forthcoming papers.

B. Flux Network

For the physiological condition of $\lambda = 35 \text{ cm}^{-1}$ [12], we compare the quantum and classical flux networks, as shown in Fig. 4. Similar to the study of the HSR model, the flux network analysis clarifies the contribution of higher-order corrections, especially multi-site quantum coherence. In the seven-site FMO model, with the barrier-crossing pathway under initial condition I, the quantum and classical trapping times are nearly the same but the detailed flux networks can be quite different: $6 \rightarrow (5, 7) \rightarrow 4 \rightarrow 3$ is the major path with a ratio of $F_{34}^C = 75\%$ in ‘classical’ hopping kinetics, whereas $3 \leftarrow 1 \rightarrow 2 \rightarrow 3$ dominates in quantum dynamics with $F_{31}^Q + F_{32}^Q = 71\%$. The branching probability from BChl 1 to BChl 3 differs by three times, $F_{31}^Q/F_{31}^C = 3.06$, and the overall quantum-classical flux difference is $\chi_F = 32\%$. The switch of the major energy transfer path results from the quantum tunneling effect of multi-site quantum coherence. With the downhill pathway under initial condition II, the flux network structure is the same for both hopping kinetics and quantum dynamics, with a smaller difference of $\chi_F = 7\%$.

C. Robustness Against the Removal of BChl 4

To complete the quantum-classical comparison for our quantum dynamic network, we study the stability of FMO after the removal of BChl 4. As shown in Fig. 3, the change of the trapping time $\langle t \rangle$ is small enough to sustain a highly efficient energy transfer. Consistent with the HSR model, quantum dynamics always leads to a smaller trapping time than hopping kinetics. This behavior can be interpreted by replacing the removal of BChl 4 with an infinite energy barrier, $\varepsilon(\text{BChl } 4) = \infty$, so that the quantum tunneling effect is very important. As shown by the flux network analysis, BChl 4 is no longer the bottleneck site under initial condition I, and the trapping time $\langle t \rangle_Q$ is unaffected by the removal of BChl 4 over a broad range of reorganization energy. The stability analysis thus reflects the multi-site quantum coherence feature of the original energy transfer network.

VII. CONCLUSIONS AND DISCUSSION

In this paper, we continue our investigation of efficient energy transfer in light-harvesting systems and compare the prediction of the trapping time and the population flux calculated by full quantum dynamics and by ‘classical’ hopping kinetics. The classical white noise (the HSR model) and the quantum Debye noise are used to model the protein environment. The quantum dynamics under the quantum Debye noise is solved by the hierarchy equation, which compares well to the GBR equation used in our first paper [6]. Relative to the rigorous results of quantum dynamics, hopping kinetics is consistently calculated by Fermi’s golden rule rate. In principle, full quantum dynamics can be mapped to an equivalent kinetic network of population transfer by a systematic expansion. We have extended the systematic expansion from the HSR model [20] to a general quantum dynamic network, which will be shown in a forthcoming paper [31]. In this mapping, the leading-order hopping rate is equivalent to Fermi’s golden rule (i.e., the Forster rate for the dipole-dipole interaction) and is taken as the ‘classical’ hopping limit. Therefore, our quantum-classical comparison is capable of systematically illustrating nontrivial quantum effects using higher-order corrections beyond the second-order truncation with the Born approximation. Our result is different from a previous approach based on factorizing the Liouville operator of various dynamic processes [22]. In the HSR model, higher-order effects originate purely from multi-site quantum coherence (direct interconversion of off-diagonal density matrix elements) [20]. For a quantum bath model such as the Debye spectral density, there exist additional contributions from bath relaxation (non-Markovianity excluding the Born approximation) [52] and the finite temperature effect [31].

Our investigation of the average trapping time demonstrates that hopping kinetics compares well with full quantum dynamics, and that the Forster rate can reliably predict optimal energy transfer in the seven-site FMO model. Two initial conditions, BChl 1 and BChl 6, are used in our study, while the initial condition is shifted to BChl 8 in the eight-site model [9]. For both the HSR model and the Debye spectral density, the quantum and classical trapping times are close, differing a few percentages over a broad range of parameters around the optimal and physiological conditions. In the local site basis, the energy difference (Δ) between two neighboring levels is several times larger than their electronic coupling (J). The study in our first paper suggests that an intermediate dissipation strength (Γ), is necessary

for the optimal energy transfer. A crude estimation on the kinetic expansion parameter, $J^2/(\Delta^2 + \Gamma^2) < 1$, indicates that quantum-classical difference can be treated as a small correction to the leading-order ‘classical’ kinetics in the overall dynamic behavior, i.e., the trapping time and the transfer efficiency.

However, nontrivial quantum coherent effects can be fundamentally important in the detailed behavior of the energy transfer process. A better measurement of nontrivial quantum effects involves off-diagonal coherence ($\rho_{mn(\neq n)}$) of the reduced density matrix. In this paper, we propose a new measure, the integrated population flux (or equivalently the branching probability), which is defined using the decay time of the off-diagonal density matrix elements ρ_{mn} in full quantum dynamics. The flux thus defined obeys the conservation law and is a unique measure of non-equilibrium energy flow in quantum networks. Through the flux network analysis, we are able to extract the two major energy transfer pathways, $1 \rightarrow 2 \rightarrow 3$ (path A) and $6 \rightarrow (5, 7) \rightarrow 4 \rightarrow 3$ (path B), in the seven-site FMO model. Here the energy transfer through path A crosses a barrier at BChl 2; path B is a downhill structure, thus becoming the dominant pathway in hopping kinetics. With the initial population at BChl 1 and the physiological condition of the Debye spectral density for the bath, the quantum tunneling effect switches the dominant pathway from path B to path A. The trapping time and flux network with the initial population at BChl 6 are much less affected due to its downhill structure. The quantum-classical comparison of the flux network thus characterizes multi-site quantum coherence for various network structures, and this coherence becomes more pronounced with the decrease of temperature. As discussed in Appendix. C, the two-pathway energy transfer structure can be found in the eight-site FMO model but the weight of the two pathways is changed due to the change of the Hamiltonian and the presence of the eighth BChl.

Using the leading-order ‘classical’ kinetics, we present a simple estimation on the stability of energy transfer against the change of internal and external parameters. The time scale separation of energy trap and decay processes, $k_d\langle t \rangle \sim 0.01$, is a key factor for FMO. Based on the estimation of hopping rate, a noticeable change in the transfer efficiency requires a dramatic change in the trapping time, which in turn requires one or two orders of magnitude change in various parameters. To induce a permanent damage in FMO, we remove the bottleneck site, BChl 4, and explore the modified trapping time in both quantum dynamics and ‘classical’ kinetics. We observe that the multiple pathways help FMO sustain a less

dramatic change in the trapping time, thus ensuring the robustness of quantum energy transfer.

Our analysis is based on a physically-motivated kinetic mapping of quantum dynamics. The quantum coherence has been discussed in the framework of the long-lived quantum beat and entanglement [37]. Complementary to these studies, we provide a quantitative measurement rather than a qualitative description for nontrivial higher-order quantum effects. Using the two-pathway FMO as our model system, we reveal the contribution of multi-site quantum coherence and its dependence on the pathway structure. Our approach can be easily applied to other light-harvesting systems and artificial devices. Specifically, multi-site quantum coherence can lead to various phenomena, e.g., quantum interference between various energy transfer pathways, quantum phase modulation of a closed transfer loop, and long-range energy exchange by quantum tunneling [20]. To systematically study these nontrivial quantum behaviors as well as the bath relaxation effect [52], we need to develop a more detailed partition procedure based on our kinetic mapping technique [31]. Our study is limited in the initial condition with pure populations, and a more general case with initial coherence will be extended in the future. For the FMO system, different Hamiltonian models have been applied in theoretical and experimental studies [44, 45]. The variation of the Hamiltonian will lead to different results, e.g., the site energy of the additional eighth BChl can be optimized close to the experimental value [9], but our quantum-classical comparison strategy is applicable in general to these new models. As a demonstration, the calculation of the eight-site model is summarized in Appendix C, where the generality of our methodology should be not confused with model-dependent results.

Acknowledgments

This work was supported by grants from the National Science Foundation (Grant CHE-1112825), DARPA (Grant N66001-10-1-4063). Jianshu Cao and late Bob Silbey were partly supported by the Center for Excitonics, an Energy Frontier Research Center funded by the US Department of Energy, Office of Basic Energy Sciences (Grant de-sc0001088). JW acknowledges partial support from the Fundamental Research Funds for the Central Universities in China (Grant 2011QNA3005) and the National Science Foundation of China (Grant 21173185).

Appendix A: Quantum Effective Kinetic Rate Matrix

In this appendix, we will provide a formal approach of kinetic mapping, and prove that the leading-order hopping rate of the HSR model can be recovered from Fermi's golden rule rate with a classical white noise.

For a kinetic network satisfying the master equation in Eq. (7), the integrated residence time is calculated by the Laplace transform

$$\hat{P}(z=0) = [K + K_t]^{-1} P(t=0), \quad (\text{A1})$$

where $\hat{P}(z) = \int_0^\infty dt e^{-zt} P(t)$ and $\tau_n = [\hat{P}(z=0)]_n$. For a quantum dynamic network, we will generate its kinetic mapping by the constraint of the same integrated residence time $\hat{P}(z=0)$. The Liouville equation, $\dot{\rho}(t) = -\mathcal{L}\rho(t)$, is rewritten as

$$\begin{aligned} \dot{\rho}_P(t) &= -\mathcal{L}_{\text{sys};PC}\rho_C(t) - \mathcal{L}_{\text{trap};P}\rho_P(t) \\ \dot{\rho}_C(t) &= -\mathcal{L}_{\text{sys};CP}\rho_P(t) - [\mathcal{L}_{\text{sys};C} + \mathcal{L}_{\text{dissp};C} + \mathcal{L}_{\text{trap};C}]\rho_C(t) \end{aligned} \quad (\text{A2})$$

where the indices P and C represent diagonal population elements and off-diagonal coherence elements of the density matrix in the local site basis. The reduced density matrix ρ is separated into two block elements, ρ_P and ρ_C . Each Liouville superoperator (\mathcal{L}_{sys} , $\mathcal{L}_{\text{trap}}$, and $\mathcal{L}_{\text{dissp}}$), is also separated into the block-matrix form. In the HSR model, the dissipation Liouville superoperator is described the pure dephasing constant Γ^* , i.e., $\mathcal{L}_{\text{dissp};C} = \Gamma^*$. In general, the influence of $\mathcal{L}_{\text{dissp};C}$ can be described by a time-convolution form, i.e., $\mathcal{L}_{\text{dissp};C}\rho_C(t) = \int_0^t M(t-\tau)\rho_C(\tau)d\tau$. The time-nonlocal dissipation kernel $M(t)$ can be formally expressed in terms of projection operators. Applying the Laplace transform, we obtain a closed form for the population vector,

$$\begin{aligned} \hat{\rho}_P(z) &= \left\{ z - \mathcal{L}_{\text{sys};PC} \left[z + \mathcal{L}_{\text{sys};C} + \hat{M}(z=0) + \mathcal{L}_{\text{trap};C} \right]^{-1} \mathcal{L}_{\text{sys};CP} + \mathcal{L}_{\text{trap};P} \right\}^{-1} \\ &\quad \times \rho_P(t=0), \end{aligned} \quad (\text{A3})$$

where $\hat{\rho}_P(z)$ and $\hat{M}(z)$ are the population vector and the dissipation Liouville superoperator in the Laplace z -domain, respectively. To derive the above equation, we presume zero initial quantum coherence, $\rho_C(t=0) = 0$. With two identities, $P = \rho_P$ and $K_t = \mathcal{L}_{\text{trap};t}$, the integrated residence time vector from the full quantum dynamics is given by

$$\hat{P}(z=0) = \left\{ -\mathcal{L}_{\text{sys};PC} \left[\mathcal{L}_{\text{sys};C} + \hat{M}(z=0) + \mathcal{L}_{\text{trap};C} \right]^{-1} \mathcal{L}_{\text{sys};CP} + K_t \right\}^{-1} P(t=0). \quad (\text{A4})$$

Comparing Eq. (A1) and Eq. (A4), we obtain the quantum kinetic rate matrix as

$$K^Q = -\mathcal{L}_{\text{sys};PC} \left[\mathcal{L}_{\text{sys};C} + \hat{M}(z=0) + \mathcal{L}_{\text{trap};C} \right]^{-1} \mathcal{L}_{\text{sys};CP}, \quad (\text{A5})$$

which includes the leading-order 'classical' hopping rates and higher-order corrections from multi-site quantum coherence. The effective quantum rate is given by $k_{mn(\neq m)}^Q = -[K^Q]_{mn}$.

In the leading order, we ignore the off-diagonal elements of $\mathcal{L}_{\text{sys};C}$, i.e., $\mathcal{L}_{\text{sys};C} \approx \mathcal{L}_{\text{sys};C}^{(0)} \rightarrow i\Delta_{mn}$. With the explicit form of \mathcal{L}_{sys} in Eq. (3), this simplification allows us to obtain the 'classical' hopping rate k_{mn}^C ($\neq k_{mn}^Q$) in Eq. (12) for the HSR model. In a forthcoming paper [31], we will demonstrate the mapping procedure for the general quantum dynamic network. The leading-order hopping rate is given by Fermi's golden rule rate in Eq. (14). For a classical white noise described by $J(\omega) = (\beta\Gamma^*/2\pi)\omega$, we ignore the constant imaginary part of $g(t)$ and arrive at

$$g(t) \approx 2 \int_0^\infty d\omega \frac{(\beta\Gamma^*/2\pi)\omega}{\omega^2} \frac{2}{\beta\omega} (1 - \cos \omega t) = \Gamma^* t \quad (\text{A6})$$

and

$$k_{m \neq n}^C = 2|J_{mn}|^2 \text{Re} \int_0^\infty d\tau e^{-(\Gamma_{mn} + i\Delta_{mn})\tau} = 2|J_{mn}|^2 \frac{\Gamma_{mn}}{\Gamma_{mn}^2 + \Delta_{mn}^2}, \quad (\text{A7})$$

which recovers the result in the HSR model.

Appendix B: Derivation of Quantum Integrated Population Flux

The integrated population flux F_{mn}^C in a classical kinetic network is defined in Eq. (9). The corresponding quantity, F_{mn}^Q , in a quantum kinetic network is similarly defined using k^Q and τ^Q . Since the quantum effective rate k^Q is difficult to be exactly determined, we will rewrite F_{mn}^Q using the time integration of coherence. Applying the Laplace transform to the second equation of Eqs. (A2) and setting the Laplace variable to be zero ($z=0$), we obtain

$$-\mathcal{L}_{\text{sys};CP} \hat{\rho}_P(0) = \left[\mathcal{L}_{\text{sys};C} + \hat{M}(z=0) + \mathcal{L}_{\text{trap};C} \right] \hat{\rho}_C(0), \quad (\text{B1})$$

where the condition of zero initial quantum coherence ($\rho_C(t=0) = 0$) is used. The above equation be further rearranged, giving

$$K^Q \hat{P}(0) = \mathcal{L}_{\text{sys};PC} \hat{\rho}_C(0) \quad (\text{B2})$$

with the help of K^Q defined in Eq. (A5). The n -th vector element on the both sides of this equation is written as

$$\sum_{m(\neq n)} [k_{mn}^Q \tau_n^Q - k_{nm}^Q \tau_m^Q] = i \sum_{m(\neq n)} (J_{nm} \tau_{mn}^Q - J_{mn} \tau_{nm}^Q), \quad (\text{B3})$$

where the coherence decay time $\tau_{mn}^Q = \int_0^\infty dt \rho_{mn}(t)$ is introduced. Since the indices, m and n , are arbitrary in the above summation, we obtain the quantum population flux as

$$F_{mn}^Q = k_{mn}^Q \tau_n^Q - k_{nm}^Q \tau_m^Q = 2 \text{Im} [J_{mn} \tau_{nm}^Q], \quad (\text{B4})$$

with two identities, $J_{nm} = J_{mn}^*$ and $\tau_{nm}^Q = [\tau_{mn}^Q]^*$.

Appendix C: Summary of Quantum-Classical Comparison and Flux Network Analysis for the Eight-Site FMO Model

Since the last year, the crystal structure of FMO has been revisited and a new eight-site model has been proposed [45]. The additional eighth BChl is considered as the initial site for energy transfer in FMO. Quantum dynamics in the original seven-site model is modified, leading to different observations. In the third paper of this series [9], we explained the suppressed oscillation in the eight-site FMO model and proposed an optimal equally-spaced ladder structure for the $8 \rightarrow (1, 2) \rightarrow 3$ pathway. Our methodology of quantum-classical comparison and flux network analysis is however general and model independent. Here we provide a short summary of our calculation for the eight-site model for the completeness.

Applying the Hamiltonian of the eight-site model from Ref. [45], which can be found in the third paper of this series [9], we perform the quantum (hierarchical equation) and classical (Fermi's golden rule rate) calculations described in Sec. VI. The bath is modeled by the Debye spectral density with the same set of parameters ($\lambda = 35 \text{ cm}^{-1}$, $1/D = 50 \text{ fs}$ and $T = 300 \text{ K}$). The high-temperature approximation is used to reduce the numerical cost. The resulting two trapping times are $\langle t \rangle_C = 4.05 \text{ ps}$ and $\langle t \rangle_Q = 4.69 \text{ ps}$, with the relative difference of $\sim 14\%$ between quantum dynamics and hopping kinetics. Compared to the result of the initial condition at BChl 1 in the seven-site FMO model, the difference of $\langle t \rangle_Q$ is less than 5%, indicating the stability of energy transfer efficiency against the change of the Hamiltonian. Next we construct the flux network using both quantum and classical approaches. As shown in Fig. 5, the two major energy transfer pathways, $8 \rightarrow 1 \rightarrow 2 \rightarrow 3$ and $6 \rightarrow (5, 7) \rightarrow 4 \rightarrow 3$,

are determined by relevant net population flows (> 0.1), and the overall structure of the flux network is kept the same under quantum and classical descriptions. The average difference between the two flux networks is $\chi_F \approx 20\%$, slightly larger than the difference of the trapping time. Compared to the case of the initial condition at BChl 1 in the seven-site model, the energy transfer in the eight-site model is more dispersed in the network, and the probabilities of the two pathways are closer ($F_{32} \approx F_{34}$). A small but unidirectional inter-path energy flow can be observed from the first pathway, $8 \rightarrow (1, 2) \rightarrow 3$, to the second pathway, $6 \rightarrow (5, 7) \rightarrow 4 \rightarrow 3$. These two phenomena are related to the Hamiltonian used in the eight-site model: 1) the average energy level of the first pathway is higher than that of the second pathway; 2) the coupling between the trap site, $J_{34} \approx 2J_{32}$, prefers the second pathway, especially in the classical description; 3) the additional eighth site allows more chances of inter-path energy flows and further increases the dispersibility. On the other hand, quantum-classical comparison also reveals a noticeable change in the weights of the two pathways ($\chi_F \approx 20\%$). Quantum mechanically, the multi-site quantum coherence allows a long-range direct energy transfer from BChl 8 to BChl 2. The increase of quantum branch probability from BChl 2 to BChl 3 compared to the classical value results from the interplay of multi-site quantum coherence and solvent relaxation effect.

In a summary, we apply the quantum-classical comparison and the flux network analysis to a new eight-site FMO model. The basic two-pathway energy transfer structure can be still observed in the eight-site FMO model. Because of the change in the Hamiltonian, the detailed results of quantum-classical difference and non-trivial quantum effects are modified accordingly. Interestingly, energy transfer becomes more dispersed in the eight-site FMO model, which may help the system resist damages.

-
- [1] R. E. Blankenship, D. M. Tiede, J. Barber, G. W. Brudvig, G. M. Fleming, M. Ghirardi, M. R. Gunner, W. Junge, D. M. Kramer, A. Melis, T. A. Moore, C. C. Moser, D. G. Nocera, A. J. Nozik, D. R. Ort, W. W. Parson, R. C. Prince, and R. T. Sayre, *Science* **332**, 805 (2011).
 - [2] G. S. Engel, T. R. Calhoun, E. L. Read, T. K. Ahn, T. Mancal, Y. C. Cheng, R. E. Blankenship, and G. R. Fleming, *Nature* **446**, 782, (2007).
 - [3] G. Panitchayangkoon, D. Hayes, K. A. Fransted, J. R. Caram, E. Harel, J. Wen, R. E.

- Blankenship, and G. S. Engel, Proc. Natl. Acad. Sci. (USA) **107**, 12766 (2010).
- [4] E. Collini, C. Y. Wong, K. E. Wilk, P. M. G. Curmi, P. Brumer, and G. D. Scholes, Nature **463**, 644 (2010).
- [5] J. S. Cao, J. Chem. Phys. **107**, 3204 (1997).
- [6] J. L. Wu, F. Liu, Y. Shen, J. S. Cao, and R. J. Silbey, New J. Phys. **12**, 105012 (2010).
- [7] A. Shabani, M. Mohseni, H. Rabitz, and S. Lloyd, arXiv:1103.3823 (2011).
- [8] M. Mohseni, A. Shabani, S. Lloyd, and H. Rabitz, arXiv:1104.4812 (2011).
- [9] J. Moix, J. L. Wu, P. F. Huo, D. F. Coker, and J. S. Cao, J. Phys. Chem. Lett. **2**, 3045 (2011).
- [10] Y. Tanimura and R. Kubo, J. Phys. Soc. Jpn. **58**, 101 (1989).
- [11] A. Ishizaki and G. R. Fleming, J. Chem. Phys. **130**, 234110, 234111 (2009).
- [12] A. Ishizaki and G. R. Fleming, Proc. Natl. Acad. Sci. (USA) **106**, 17255 (2009).
- [13] Y. Yan, F. Yang, Y. Liu, and J. Shao, Chem. Phys. Lett. **395**, 216 (2004).
- [14] L. P. Chen, R. H. Zheng, Y. Y. Jing, and Q. Shi, J. Chem. Phys. **134**, 194508 (2011).
- [15] B. Palmieri, D. Abramavicius, and S. Mukamel, J. Chem. Phys. **130**, 204512 (2009).
- [16] P. F. Huo and D. F. Coker, J. Phys. Chem. Lett. **2**, 825 (2011).
- [17] H. Haken and P. Reineker, Z. Physik **249**, 253 (1972).
- [18] H. Haken and G. Strobl, Z. Physik **262**, 135 (1973).
- [19] R. J. Silbey, Ann. Rev. Phys. Chem. **27**, 203 (1976).
- [20] J. S. Cao and R. J. Silbey, J. Phys. Chem. A **113**, 13825 (2009).
- [21] X. Chen and R. J. Silbey, J. Phys. Chem. B **115**, 5499 (2011).
- [22] P. Rebentrost, M. Mohseni, and A. Aspuru-Guzik, J. Phys. Chem. B **113**, 9942 (2009).
- [23] R. Rebentrost, M. Mohseni, I. Kassal, S. Lloyd, and A. Aspuru-Guzik, New J. Phys. **11**, 033003 (2009).
- [24] M. B. Plenio and S. F. Huelga, New J. Phys. **10**, 113019 (2008).
- [25] F. Caruso, A. W. Chin, A. Datta, S. F. Huelga, and M. B. Plenio, J. Chem. Phys. **131**, 105106 (2009).
- [26] S. Yang, D. Z. Xu, Z. Song, and C. P. Sun, J. Chem. Phys. **132**, 234501 (2010).
- [27] M. Yang, and G. R. Fleming, Chem. Phys. **282**, 163 (2002).
- [28] A. Ishizaki and G. R. Fleming, J. Phys. Chem. B **115**, 6227 (2011)
- [29] M. Aghtar, J. Liebers, J. Strumpfer, K. Schulten, and U. Kleinekathofer J. Chem. Phys. **136**, 214101 (2012).

- [30] T. C. Berkelbach, T. E. Markland, and D. R. Reichman, *J. Chem. Phys.* **136**, 084104 (2012).
- [31] J. L. Wu, R. J. Silbey, and J. S. Cao, to be submitted.
- [32] C. Kreisbeck, T. Kramer, M. Rodriguez, and B. Hein, *J. Chem. Theor. Comp.* **7**, 2166 (2011).
- [33] J. L. Wu, R. J. Silbey, and J. S. Cao, submitted (2012).
- [34] J. S. Cao, *J. Phys. Chem. B* **115**, 5493 (2011).
- [35] J. L. Wu and J. S. Cao, *Adv. Chem. Phys.* **146**, 329 (2011).
- [36] N. G. van Kampen, *Stochastic Processes in Physics and Chemistry* (Elsevier Science, New York, 1992).
- [37] M. Sarovar, A. Ishizaki, G. R. Fleming, and K. B. Whaley, *Nat. Phys.* **6**, 462 (2010).
- [38] V. May and K. Oliver, *Charge and Energy Transfer Dynamics in Molecular Systems* (Wiley-VCH, Weinheim, 2004).
- [39] U. Ermler, G. Fritzsche, S. K. Buchanan, and H. Michel, *Structure* **2**, 925 (1994).
- [40] Y. F. Li, W. Zhou, R. E. Blankenship, and J. P. Allen, *J. Mol. Biol.* **271**, 456 (1997).
- [41] S. I. E. Vulto, M. A. de Baat, R. J. W. Louwe, H. P. Permentier, T. Neef, M. Miller, H. van Amerongen, and T. J. Aartsma, *J. Phys. Chem. B* **102**, 9577 (1998).
- [42] M. Cho, H. M. Vaswani, T. Brixner, J. Stenger, and G. R. Fleming, *J. Phys. Chem. B* **109**, 10542 (2005).
- [43] T. Brixner, J. Stenger, H. M. Vaswani, M. Cho, R. E. Blankenship, and G. R. Fleming, *Nature* **434**, 625 (2005).
- [44] J. Adolphs, and T. Renger, *Biophys. J.* **91**, 2778 (2006).
- [45] M. S. A. Busch, F. Müh, M. E. Madjet, and T. Renger, *J. Phys. Chem. Lett.* **2**, 93 (2011).
- [46] S. Mukamel, *Principles of Nonlinear Optical Spectroscopy* (Oxford University Press, New York, 1995).
- [47] A. Nitzan, *Chemical Dynamics in Condensed Phases: Relaxation, Transfer and Reactions in Condensed Molecular Systems* (Oxford University Press, New York, 2006).
- [48] J. S. Cao, L. W. Ungar, and G. A. Voth, *J. Chem. Phys.* **104**, 4189 (1996).
- [49] S. Hoyer, M. Sarovar, and K. B. Whaley, *New J. Phys.* **12**, 065041 (2010).
- [50] J. H. Kim and J. S. Cao, *J. Phys. Chem. B* **114**, 16189 (2010).
- [51] S. Hoyer, A. Ishizaki, and K. B. Whaley, arXiv:1106.2911.
- [52] J. S. Cao, *J. Chem. Phys.* **112**, 6719 (2000).
- [53] J. M. Moix, Y. Zhao, and J. S. Cao, *Phys. Rev. B* **85**, 115412 (2012).

Figure Captions

Fig. 1: The average trapping time $\langle t \rangle$ vs. the pure dephasing rate Γ^* in the HSR model of the seven-site FMO for a) the initial population at BChl 1, and b) the initial population at BChl 6. The solid curves are calculated from full quantum dynamics, whereas the dashed curves are calculated from the leading-order ‘classical’ kinetics. In each figure, the lower pair of curves correspond to the seven-site FMO model, while the upper pair corresponds to the six-site FMO model after the removal of BChl 4.

Fig. 2: The flux networks of FMO under the optimal pure dephasing rate in the HSR model of the seven-site FMO for a) initial population at BChl 1 ($\Gamma_{\text{opt}}^* = 175 \text{ cm}^{-1}$), and b) initial population at BChl 6 ($\Gamma_{\text{opt}}^* = 195 \text{ cm}^{-1}$). For each population flux, the upper number is obtained from full quantum dynamics, whereas the lower number is obtained from the leading-order hopping kinetics.

Fig. 3: The average trapping time $\langle t \rangle$ of the seven-site FMO vs. the reorganization energy λ of the Debye spectral density for a) the initial population at BChl 1, and b) the initial population at BChl 6. The other bath parameters are given in text. The solid curves are results of full quantum dynamics, whereas the dashed curves results of the leading-order hopping kinetics. In each figure, the lower pair of curves (black) correspond to the seven-site FMO model, while the upper pair (red) corresponds to the six-site FMO model with the removal of BChl 4. (colored online)

Fig. 4: The flux networks of the seven-site FMO under the physiological condition ($\lambda = 35 \text{ cm}^{-1}$, $1/D = 50 \text{ fs}$, and $T = 300 \text{ K}$) of the Debye spectral density for a) initial population at BChl 1, and b) initial population at BChl 6. For each population flux, the upper number is obtained using full quantum dynamics whereas the lower number is obtained using the leading-order ‘classical’ hopping kinetics.

Fig. 5: The flux networks of the eight-site FMO under the physiological condition ($\lambda = 35 \text{ cm}^{-1}$, $1/D = 50 \text{ fs}$, and $T = 300 \text{ K}$) of the Debye spectral density using a) full quantum dynamics and b) the leading-order classical kinetics.

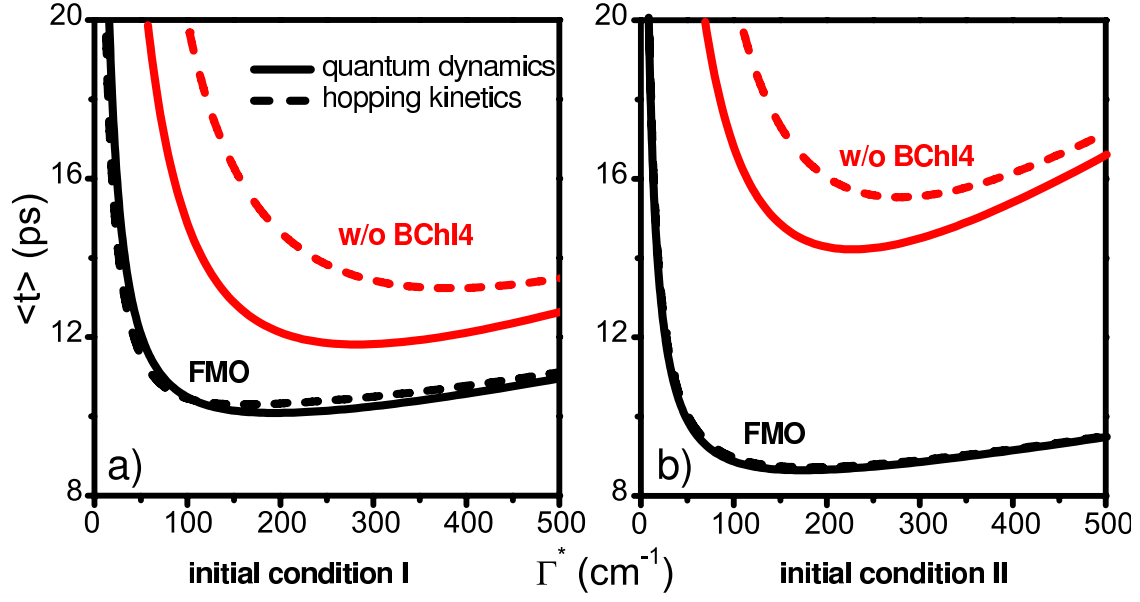


FIG. 1: The average trapping time $\langle t \rangle$ vs. the pure dephasing rate Γ^* in the HSR model of the seven-site FMO for a) the initial population at BChl 1, and b) the initial population at BChl 6. The solid curves are calculated from full quantum dynamics, whereas the dashed curves are calculated from the leading-order ‘classical’ kinetics. In each figure, the lower pair of curves correspond to the seven-site FMO model, while the upper pair corresponds to the six-site FMO model after the removal of BChl 4.

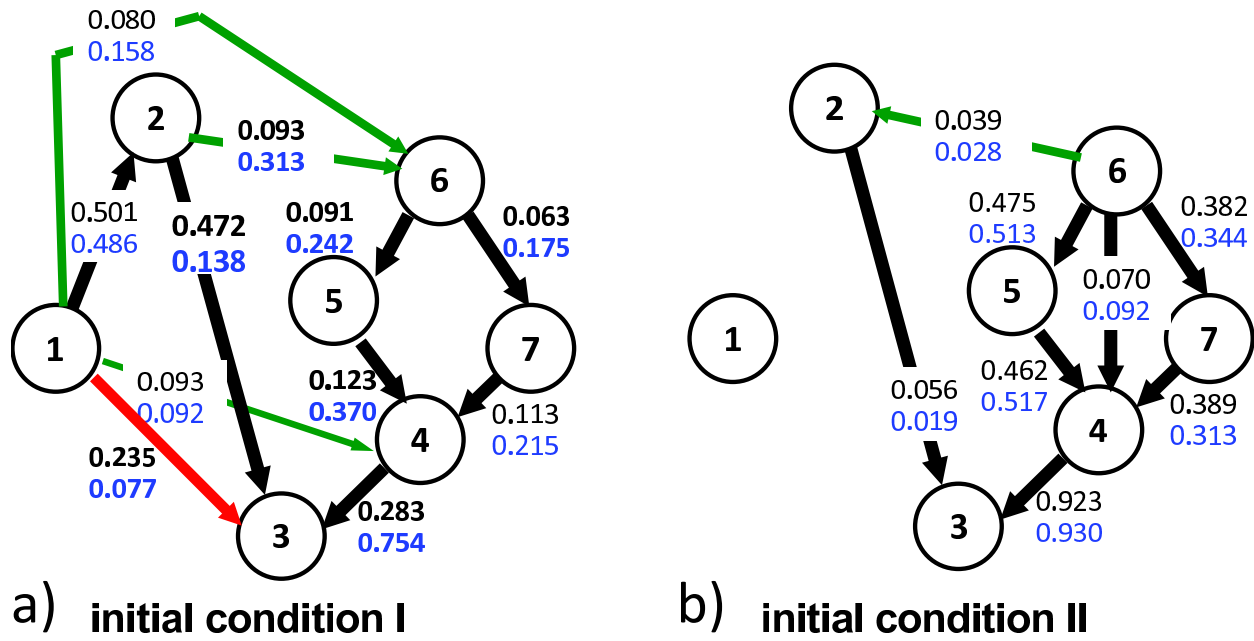


FIG. 2: The flux networks of FMO under the optimal pure dephasing rate in the HSR model of the seven-site FMO for a) initial population at BChl 1 ($\Gamma_{\text{opt}}^* = 175 \text{ cm}^{-1}$), and b) initial population at BChl 6 ($\Gamma_{\text{opt}}^* = 195 \text{ cm}^{-1}$). For each population flux, the upper number is obtained from full quantum dynamics, whereas the lower number is obtained from the leading-order hopping kinetics.

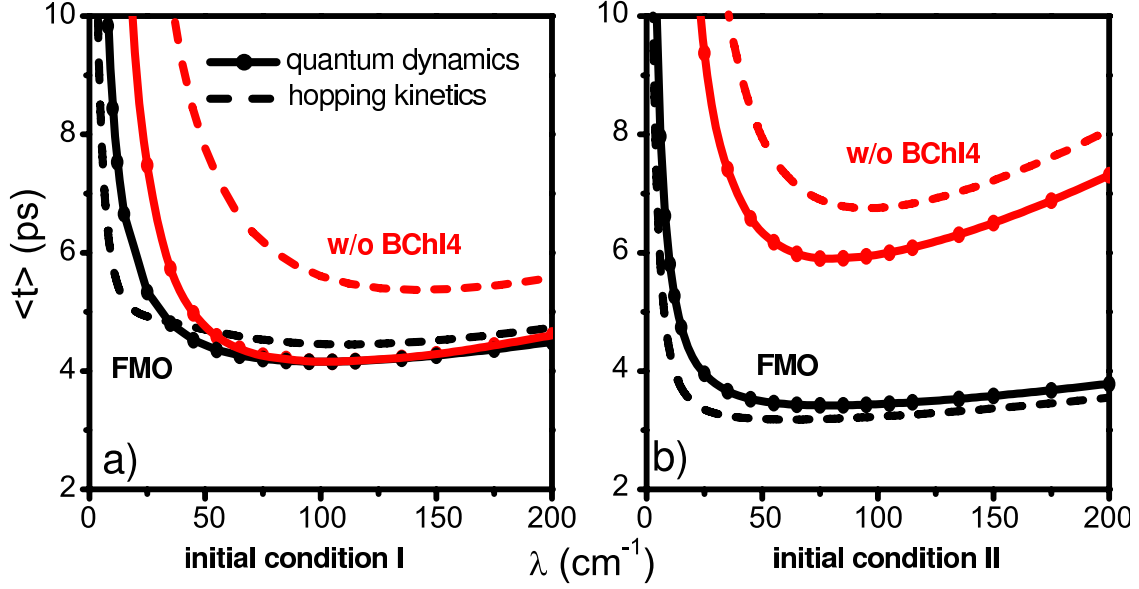


FIG. 3: The average trapping time $\langle t \rangle$ of the seven-site FMO vs. the reorganization energy λ of the Debye spectral density for a) the initial population at BChl 1, and b) the initial population at BChl 6. The other bath parameters are given in text. The solid curves are results of full quantum dynamics, whereas the dashed curves results of the leading-order hopping kinetics. In each figure, the lower pair of curves (black) correspond to the seven-site FMO model, while the upper pair (red) corresponds to the six-site FMO model with the removal of BChl 4. (colored online)

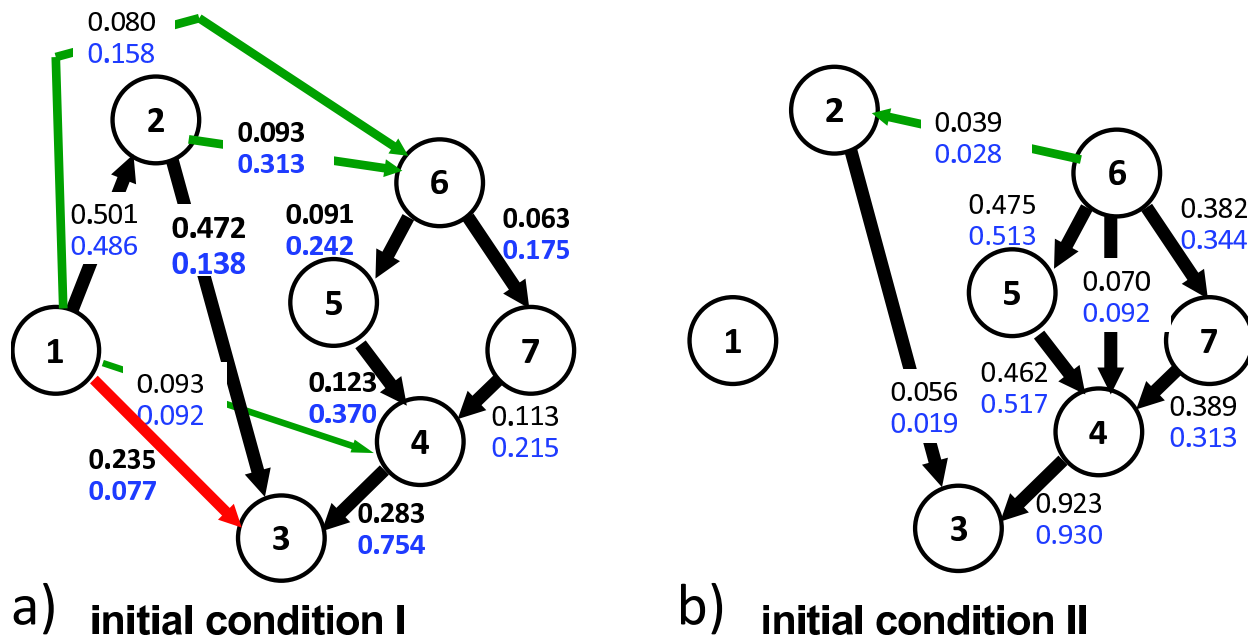


FIG. 4: The flux networks of the seven-site FMO under the physiological condition ($\lambda = 35 \text{ cm}^{-1}$, $1/D = 50 \text{ fs}$, and $T = 300 \text{ K}$) of the Debye spectral density for a) initial population at BChl 1, and b) initial population at BChl 6. For each population flux, the upper number is obtained using full quantum dynamics whereas the lower number is obtained using the leading-order ‘classical’ hopping kinetics.

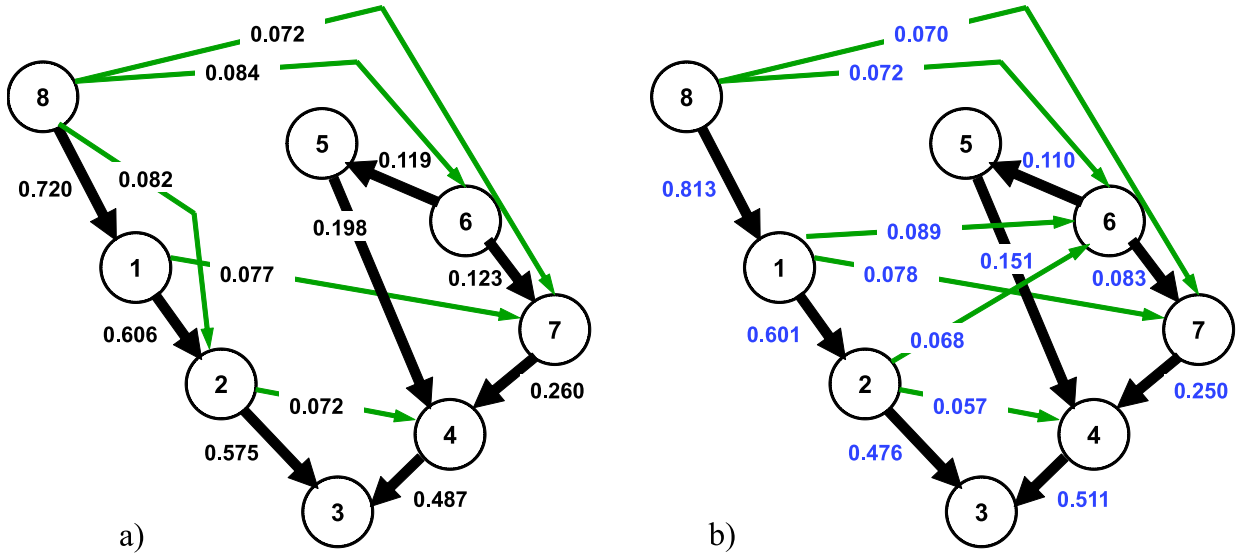


FIG. 5: The flux networks of the eight-site FMO under the physiological condition ($\lambda = 35 \text{ cm}^{-1}$, $1/D = 50 \text{ fs}$, and $T = 300 \text{ K}$) of the Debye spectral density using a) full quantum dynamics and b) the leading-order classical kinetics.